RSC Advances

PAPER

View Article Online
View Journal | View Issue



Cite this: *RSC Adv.*, 2026, **16**, 22564

# Design of polar $XC_3$ (X = P, As, Sb, Bi) monolayers with coupled bandgap, polarization, and optical responses

Wenxiao Li,†[a] Junlan Shi,†[a] Jing Chang *[b] and Botao Fu *[a]

Bandgap engineering and polarization control in graphene-based systems are crucial for developing high-performance two-dimensional (2D) semiconductors. However, simultaneously achieving a sizable bandgap, intrinsic polarity, and strong light–matter interaction remains challenging. Here, we propose a new class of carbon-based polar semiconductors, monolayer $XC_3$ (X = P, As, Sb, Bi), designed by substituting group-V elements into graphene to break its sublattice symmetry. This symmetry breaking not only opens wide bandgaps (2.23–3.11 eV) but also induces spontaneous out-of-plane (OOP) electric polarization (−3.1–8.1 pC $m^{-1}$) and an internal electric field, stabilizing polar phases and facilitating photocarrier separation. The resulting electronic structures exhibit a distinctive Mexican-hat-shaped valence band and strong band nesting, leading to intense visible-to-near-ultraviolet optical absorption (>$10^5$ $cm^{-1}$). Moreover, $XC_3$ monolayers possess large and anisotropic carrier mobilities and exhibit band-edge alignments suitable for photocatalytic water splitting across a wide pH range (0–10). These findings establish a general route to 2D polar semiconductors that integrate coupled electronic, optical, and catalytic functionalities, offering a promising platform for graphene-derived optoelectronic and energy applications.

Received 11th January 2026
Accepted 7th April 2026

DOI: 10.1039/d6ra00272b

rsc.li/rsc-advances



## 1. Introduction

Graphene, a 2D material composed of $sp^2$-hybridized carbon atoms, exhibits exceptional electrical, mechanical, and thermal properties. However, its intrinsic zero bandgap severely restricts its applications in semiconductor and optoelectronic devices.[1–3] In contrast, 2D pnictogen monolayers—such as phosphorene, arsenene, antimonene, and bismuthene-consisting of $sp^3$-hybridized atoms, possess intrinsic semiconducting behavior with tunable band gaps and high on/off ratios.[4–10] Nevertheless, the high chemical reactivity of phosphorene leads to poor environmental stability, which greatly limits its practical device applications.[11–13]

2D carbon–pnictogen compounds have attracted increasing attention due to their structural tunability and versatile electronic properties, enabled by the combination of robust $sp^2$ C–C bonding and the flexible coordination chemistry of group-V elements.[14,15] First-principles studies have revealed diverse structural phases with intriguing chemical bonding and band dispersions, demonstrating the promise of carbon–pnictogen hybrids for applications in nanoelectronics and optoelectronics.[16,17] In particular, phosphorus carbide (CP) monolayers have been extensively explored. Wang *et al.* predicted three stable CP allotropes (α-, β-, and γ-CP) exhibiting high carrier mobilities and Dirac semimetallic states,[16] while Guan *et al.* reported additional polymorphs spanning metallic to semiconducting behaviors,[18] illustrating the structural richness of P–C bonding networks.

Theoretical progress has been supported by experimental validation. Tan *et al.* synthesized few-layer α-CP *via* carbon doping of black phosphorus,[19] and the measured hole mobility (1995 $cm^2$ $V^{-1}$ $s^{-1}$) agrees well with theoretical predictions.[20] This breakthrough confirms the feasibility of stabilizing 2D carbon–pnictogen frameworks experimentally. Moreover, other carbon–pnictogen monolayers, including AsC, $C_3P$, $C_6P$, $CP_2$, and $CP_3$, have been theoretically proposed[21–23] and exhibit useful functionalities such as high carrier mobility, strong visible-light absorption, and appropriate band edges for photocatalytic water splitting.[13] Chemical substitution has further broadened their tunability in stability and band structure engineering.[24,25]

Despite these advances, most reported carbon–pnictogen monolayers possess centrosymmetric crystal structures,[26] which fundamentally limits their multifunctionality. Inversion symmetry suppresses spin–orbit-related effects,[27] prohibits electric spontaneous polarization,[28,29] and eliminates second-order nonlinear optical responses,[30] restricting their potential in spintronics, ferroelectric devices, and nonlinear photonics. Therefore, designing non-centrosymmetric carbon–pnictogen

[a]*College of Physics and Electronic Engineering, Center for Computational Sciences, Sichuan Normal University, Chengdu, 610068, China. E-mail: fubotao2008@gmail.com*

[b]*College of Physics and Electronic Engineering, Sichuan Normal University, Chengdu, 610068, China. E-mail: changjing0394@163.com*

† These authors contributed equally to this work.

monolayers with intrinsic polarity and tunable symmetry-breaking effects remains an open challenge.

In this work we introduce an intrinsically polar family of carbon–pnictogen monolayers, $XC_3$ (X = P, As, Sb, Bi), obtained by substitutional doping of graphene with group-V atoms. First-principles calculations show that every $XC_3$ sheet hosts spontaneous OOP electric polarization (−3.1–8.1 pC $m^{-1}$) arising from buckled polar X–C bonds. *Ab initio* molecular-dynamics runs at 300 K and vibrational analysis confirm thermal and dynamic stability. The materials are indirect-gap semiconductors (2.13–3.11 eV) that absorb strongly across the visible range. Their Mexican-hat-shaped valence bands induce pronounced band nesting, resulting in optical absorption coefficients exceeding $10^5$ $cm^{-1}$ near the band edge. Importantly, the band edges of every $XC_3$ monolayer straddle the water-splitting redox levels throughout pH 0–10, enabling concurrent $H_2$ and $O_2$ evolution. $XC_3$ thus defines a hitherto overlooked family of polar 2D semiconductors that unite robustness, intrinsic polarity, and strong visible-light response, promising for next-generation optoelectronic and energy-conversion devices.

## 2. Computational methods

First-principles calculations were conducted using density functional theory (DFT) as implemented in the Vienna *Ab initio* Simulation Package (VASP).[31–34] The generalized gradient approximation (GGA) in the Perdew–Burke–Ernzerhof (PBE) formulation was employed to account for exchange–correlation interactions.[35] For more precise electronic structure calculations, the Heyd–Scuseria–Ernzerhof (HSE06) screened hybrid functional was utilized.[36] An energy cutoff of 500 eV was applied, and full atomic relaxation was performed, with convergence criteria set to $10^{-5}$ eV for total energy and $10^{-3}$ eV $Å^{-1}$ for atomic forces.[37] A vacuum spacing of 20 Å was included along the OOP direction to prevent interlayer interactions. Brillouin zone (BZ) sampling was performed using a 12 × 12 × 1 Monkhorst–Pack grid.

## 3. Geometric structure and stability

As shown in Fig. 1(a and b), monolayer $XC_3$ (X = P, As, Sb, Bi) can be constructed by symmetrically incorporating two X atoms into a 2 × 2 graphene supercell. Each unit cell contains eight atoms: six carbon atoms forming an inner planar hexagonal lattice and two pnictogen atoms occupying the outer hexagonal sites. This high-symmetry substitution preserves the overall crystalline motif of graphene while introducing chemical modulation through the dopant atoms. A structurally analogous compound, $NC_3$, has already been experimentally synthesized,[38] indicating that $XC_3$ can be regarded as a family of $NC_3$ derivatives obtained by replacing nitrogen with heavier group-V elements.[39]

Although $XC_3$ shares a similar lattice topology with $NC_3$, its local bonding environment is distinctly different. The electron localization function (ELF) analysis in Fig. S3 in the SI[40] reveals that while $NC_3$ maintains a planar $sp^2$ hybridization, the heavier pnictogen atoms in $XC_3$ exhibit a pronounced tendency toward $sp^3$-like hybridization with neighboring carbon atoms. This hybridization character breaks planarity and drives

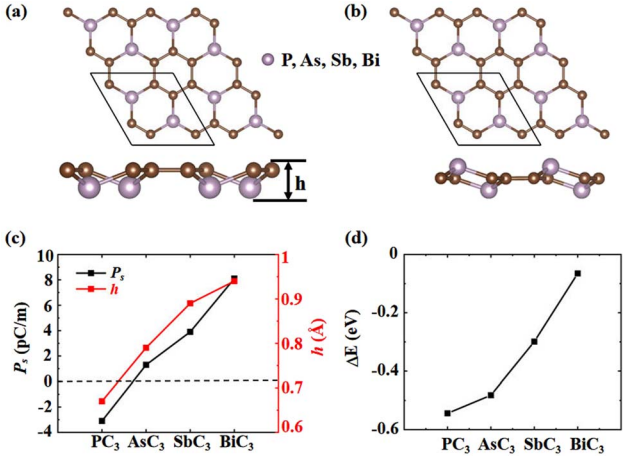


Fig. 1 (a) Top and side views of the α-$XC_3$. (b) Corresponding views of the β-$XC_3$. (c) The spontaneous electric polarization ($P_s$) and buckling height ($h$) of α-$XC_3$. (d) Energy difference ($\Delta E$) between the α and β phases.

a spontaneous OOP buckling of the lattice, forming a polar trigonal–pyramidal configuration around each pnictogen atom. Interestingly, the coexistence of two such X-centered pyramidal units per unit cell allows two possible arrangements, giving rise to the α- and β-phases.

As depicted in Fig. 1(a), the α-phase displaces both pnictogen atoms to the same side of the carbon sheet, generating a globally polar structure (space group *P6mm*) with a buckling height $h$. The trigonal–pyramidal units tilt cooperatively, producing a net OOP $P_s$. Both the $h$ (0.67–0.94 Å) and $P_s$ (−3.1–8.1 pC $m^{-1}$) increase monotonically with the pnictogen atomic number with both the $h$ and $P_s$ increase monotonically with the pnictogen atomic number [Fig. 1(c)]; notably, $PC_3$ points host opposite polarization direction to the other three monolayers. In contrast, the β-phase in Fig. 1(b) shifts the two pnictogen atoms in opposite directions, yielding a centrosymmetric, non-polar lattice with space group $P\bar{3}$ and point group $S_6$. Comparing the two phases thus demonstrates that the polarity of $XC_3$ is dictated solely by the sense of pnictogen displacement.

To determine the thermodynamically stable phase, we performed total-energy calculations for both α- and β-phases. As summarized in Fig. 1(d), the energy difference, defined as $\Delta E = E_\beta - E_\alpha$, is negative for all four $XC_3$ compounds, indicating that the α-phase is energetically favored and thus the ground state. Therefore, in the following sections, we focus on the polar α-phase of $XC_3$, which represents the most stable configuration with OOP $P_s$. Furthermore, the mechanical, dynamical, and thermodynamic stability of the α-phase is verified by phonon dispersion, *abinitio* molecular dynamics (AIMD) simulations, and the calculations of binding and formation energies, as shown in Fig. S1 and S2.

## 4. Electronic structures

HSE06 band structures and densities of states (DOS) for four carbon–pnictogen monolayers are displayed in Fig. 2. $PC_3$ and

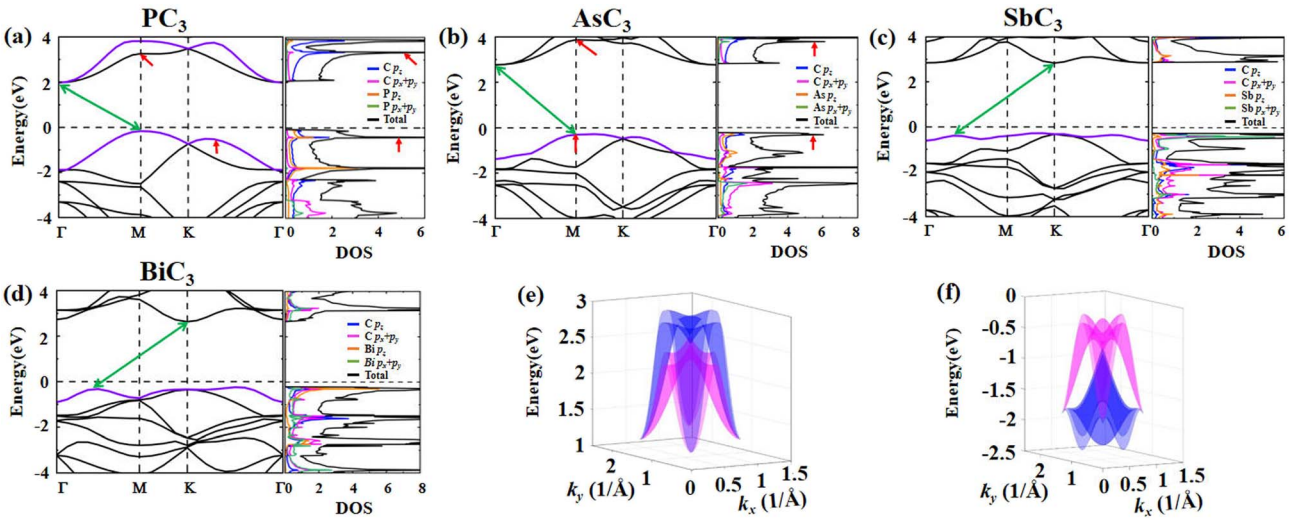


Fig. 2 (a)–(d) Band structures density of states (DOS) of the $XC_3$ monolayers. (e) 3D view of the two LCB below the Fermi level in $PC_3$. (f) 3D view of the two HVB above the Fermi level in $PC_3$.

$AsC_3$ [Fig. 2(a and b)] are indirect-gap semiconductors with the valence-band maximum (VBM) at M and the conduction-band minimum (CBM) at Γ, and the gap increases from 2.13 eV ($PC_3$) to 3.05 eV ($AsC_3$). For $SbC_3$ and $BiC_3$ [Fig. 2(c and d)] the CBM moves to K while the VBM lies along the Γ–K path, and the gap narrows to 3.11 eV ($SbC_3$) and 2.87 eV ($BiC_3$).

Projected DOS reveals the orbital character behind this evolution. For $PC_3$ and $AsC_3$ [Fig. 2(a and b)] the highest valence band (HVB) is built from C and X $p_z$ states, whereas the lowest conduction band (LCB) is dominated by C $p_z$. Moving to $SbC_3$ [Fig. 2(c)] the HVB acquires strong Sb $p_{x,y}$ weight and the LCB mixes Sb $p_z$ and C p states. In $BiC_3$ [Fig. 2(d)] the HVB is mostly Bi $p_z$ and the LCB is composed of Bi $p_{x,y}$ plus C p. Thus, with increasing atomic number of X the $p_{x,y}$ contribution to the conduction states grows at the expense of $p_z$, underscoring the strengthening of in-plane orbital hybridization.

Most importantly, all $XC_3$ display unique and distinctive band structure features: (i) the two HVBs cross at the K point, forming Dirac points akin to those observed in pristine graphene. However, due to the substitution of two X atoms in place of C atoms in $XC_3$, two additional electrons are introduced, leading to fully occupied Dirac bands, thereby inducing semiconducting behavior. Thus, the band gap opening in $XC_3$, which maintains the system's intrinsic high symmetry, fundamentally arises from alterations in electron filling. This methodology diverges from conventional band engineering techniques in graphene, which typically disrupt the system's symmetry *via* adsorption or the imposition of external fields. (ii) Of particular interest is the observation that HVBs of $PC_3$ exhibit a characteristic "Mexican hat" profile, as shown in Fig. 2(e and f). This feature is most pronounced in the band structures of $PC_3$ and $AsC_3$, while it becomes progressively less distinct in $SbC_3$ and $BiC_3$. This unique band structure significantly enhances the DOS of the HVB near the band edges. The conduction bands of $PC_3$ and $AsC_3$ also feature Dirac-like structures, as indicated by the arrows in Fig. 2(a and b), with the LCB presenting a saddle point at the M point, contributing to a pronounced DOS peak.

To further clarify the relationship between crystal structure and electronic properties, the main structural parameters and electronic characteristics—including the lattice constant ($a$), buckling height ($h$), C–X bond length ($d_{C-X}$), indirect band gap ($E_g$), and the bandwidth of the highest valence band ($\Delta E_{HVB}$)—are summarized in Table S1 of the SI. These results provide a quantitative comparison of how the electronic structures evolve with the underlying structural parameters. Overall, except for $BiC_3$, the $XC_3$ compounds exhibit clear systematic trends with increasing atomic size of X. From $PC_3$ to $SbC_3$, the lattice constant, buckling height, and C–X bond length gradually increase. Correspondingly, the band gap increases, while the bandwidth of the HVB decreases. $BiC_3$ shows a slight deviation from this trend, which can be attributed to its more complex orbital hybridization and modified electronic interactions. These results reveal a clear structure–property correlation and help elucidate the structural origin of the characteristic electronic structures in the $XC_3$ family.

## 5. Optical property

Materials possessing unconventional electronic band features, such as Van Hove singularities or Mexican-hat-like dispersions, have been shown to strongly affect charge transport and optical responses, thus offering potential for next-generation device applications. In this section, we examine the optical properties of $XC_3$ compounds as intrinsic semiconductors and show that their characteristic band structures play a decisive role in shaping the light absorption spectrum.

The optical absorption coefficient $\alpha(\omega)$ was obtained from the complex dielectric function calculated using first-principles methods.[41,42] Fig. 3(a–d) present the optical absorption spectra of $XC_3$ compounds evaluated with the HSE06 functional. For comparison, we also computed the absorption spectra of two

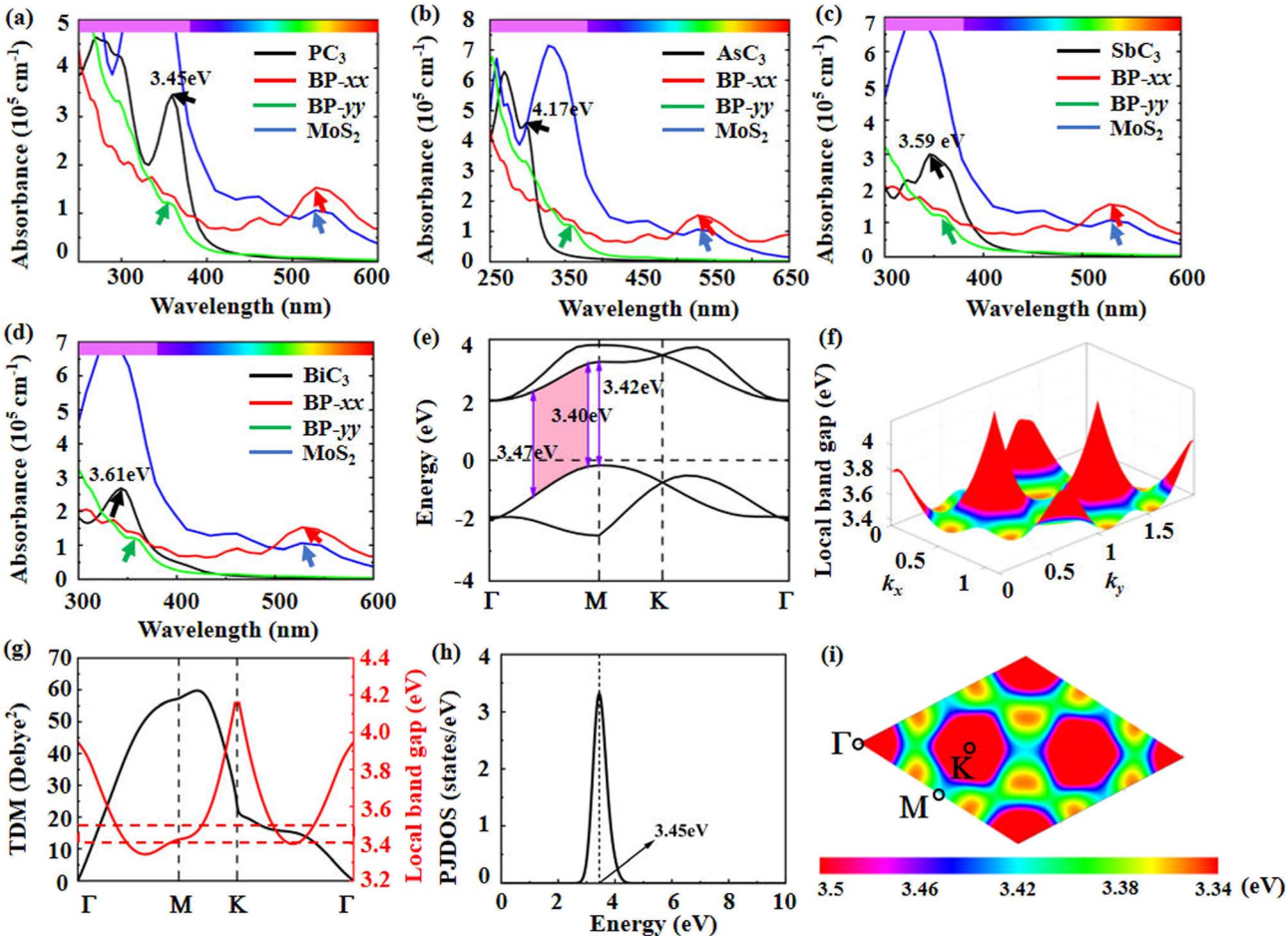


Fig. 3 (a)–(d) Optical absorption spectra of $XC_3$ monolayers. For comparison, the absorption coefficients of monolayer $MoS_2$ and black phosphorus (BP) are also shown. The arrows mark the first band-edge absorption peak. (e) Enlarged view of the $PC_3$ band structure near the Fermi level, where the shaded pink region highlights the band nesting feature. (f) Side view of the 3D distribution of the local band gap function $E_{cv}(\vec{k})$ for $PC_3$. (g) Transition dipole moment (TDM) between the highest valence band (HVB) and the lowest conduction band (LCB) of $PC_3$ (left axis), plotted together with the corresponding local band gap (right axis). (h) Partial joint density of states (JDOS) between the HVB and LCB of $PC_3$. (i) Top view of the 3D distribution of the local band gap function $E_{cv}(\vec{k})$ for $PC_3$.

widely studied 2D semiconductors, monolayer $MoS_2$ and black phosphorene.[43]

All $XC_3$ exhibit pronounced band-edge absorption peaks exceeding $10^5$ cm$^{-1}$, which are stronger than those of $MoS_2$ and black phosphorene, as indicated by the arrows in Fig. 3(a–d). Among them, $PC_3$ shows the highest absorption intensity in the visible region, with its first band-edge peak located at 3.45 eV and reaching $3.5 \times 10^5$ cm$^{-1}$. From $PC_3$ to $AsC_3$, the peak absorption intensities slightly decrease and the peak positions exhibit a systematic blue shift, moving from the blue-violet region (3.45 eV) to the near-ultraviolet region (4.17 eV), consistent with the increase in band gap. Conversely, from $SbC_3$ to $BiC_3$, a red-shift trend is observed with decreasing band gap.

To elucidate the mechanisms underlying the ultrahigh optical absorption in the $XC_3$ series, we analyze $PC_3$ as a representative example, focusing on its unique electronic band structure and interband transition probability ($W_{\vec{k}}$). For semiconductors, the absorption coefficient for direct transitions is directly related to the transition probability, which can be approximated using Fermi's golden rule.[44] This rule gives the probability per unit time that an electron undergoes a transition from an initial state $|v\rangle$ in the valence band to a final state $|c\rangle$ in the conduction band at the vector $\vec{k}$ in the Brillouin zone:

$$W_{\vec{k}} = \frac{2\pi}{\hbar}|\langle v|H'|c\rangle|^2\delta\left[E_c\left(\vec{k}\right) - E_v\left(\vec{k}\right) - \hbar\omega\right], \quad (1)$$

where $E_c(\vec{k})$ and $E_v(\vec{k})$ denote the energies of the conduction and valence bands at $\vec{k}$, respectively, and $H'$ is the perturbative Hamiltonian describing the coupling between the electromagnetic field and the electronic states. The first term represents the transition dipole moment (TDM) between the initial and final states, denoted as $M_{if}$,[45] while the second term corresponds to the joint density of states (JDOS), $J_{cv}(\hbar\omega)$:

$$J_{cv}(\hbar\omega) = \frac{2}{(2\pi)^3}\int_{E_{cv}=\hbar\omega}\frac{ds}{\left|\nabla_k E_{cv}\left(\vec{k}\right)\right|}. \quad (2)$$

Here, $E_{cv}(\vec{k}) = E_c(\vec{k}) - E_v(\vec{k})$ denotes the local band-gap function that links the conduction and valence bands. This

formulation captures the JDOS by integrating over isoenergy surfaces in momentum space. Thus, according to Fermi's golden rule, the optical absorption coefficient on a microscopic level is jointly determined by both the TDM and the JDOS.

As illustrated in Fig. 3(f and i), the 3D distribution of $E_{cv}$ exhibits a nearly flat dispersion near the M point (highlighted in green), implying that $|\nabla_{\vec{k}} E_{cv}| \approx 0$. This behavior arises from the similar dispersions of the conduction and valence bands along the Γ–M direction, where $\nabla_{\vec{k}} E_c \approx \nabla_{\vec{k}} E_v \neq 0$, resulting in a pronounced band-nesting effect in the energy range of 3.40–3.47 eV, as indicated by the pink region in Fig. 3(e). Analogous to the divergent density of states (DOS) induced by flat electronic bands, the flatness of $E_{cv}$ in the nesting region gives rise to a large JDOS contribution. In addition, the M point (3.42 eV) serves as a saddle point in the band structure, further enhancing the JDOS. This is confirmed by our DFT calculations, which reveal a pronounced JDOS peak at approximately 3.45 eV, as shown in Fig. 3(h). Therefore, the strong absorption peak originates from the combined effects of band nesting and the saddle-point singularity in $PC_3$.

In Fig. 3(g), the TDM between the HVB and LCB, along with the local bandgap distribution, are presented along the entire high-symmetry path near the Fermi level for $PC_3$. A notable finding is the presence of significantly high allowable transition probabilities near the M point. Along the M–Γ direction, the transition probability gradually decreases, reaching zero at the Γ point, where transitions are forbidden. Conversely, along the M–K direction, the probability first increases and then sharply decreases, reaching a maximum near the M point. Therefore, we infer that it is the combination of TDM and JDOS contributes to the prominent band-edge absorption, as demonstrated in Fig. 3(a). A similar analysis of $AsC_3$ is provided in the SI.

## 6. Carrier mobility

The high light absorption coefficient ensures that the 2D polar semiconductor $XC_3$ can effectively capture photons and generate a large number of photogenerated carriers. Whether these carriers can be efficiently collected and utilized also depends on their mobility within the material. Based on the deformation potential theory, the carrier mobility ($\mu_{x,y}$) can be expressed as:[46]

$$\mu_{x,y} = \frac{e\hbar^3 C_{x,y}}{k_B T m^*_{x,y} \sqrt{m^*_x m^*_y} \left(E_{x,y}{}^i\right)^2}, \quad (3)$$

where $e$ is the elementary charge, $\hbar$ is the reduced Planck constant, $k_B$ is the Boltzmann constant, $T$ is the room temperature, $m^*_{x,y}$ is the effective mass, $C_{x,y}$ is the elastic modulus and $E_{x,y}{}^i$ is the deformation potential constant for the $i$th band. The subscripts $x$ and $y$ directions correspond respectively to the armchair and zigzag transport directions.

Table 1 summarizes the relevant parameters, and the carrier mobility values for the $XC_3$ were derived using eqn (3). Unlike the isotropic and symmetric ultrahigh carrier mobility observed in graphene for both electron and hole, the $XC_3$ family display a wide range of carrier mobility, spanning from 10 to $10^5$ $cm^2$ $V^{-1}$ $s^{-1}$. More importantly, they exhibit pronounced anisotropy and significant asymmetry between electron and hole.

Table 1 The carrier mobility with relevant parameters for $XC_3$ materials, including $C_{x,y}$ (J $m^{-2}$), $m^*_{x,y}$ ($m_0$), $E_{x,y}$ (eV), and $\mu_{x,y}$ ($10^3$ $cm^2$ $V^{-1}$ $s^{-1}$). The $m_0$ is the rest mass of electron. The VA refers to different group VA elements and e/h stands for electron/hole carrier

| VA | e/h | $C_x$ | $C_y$ | $m^*_x$ | $m^*_y$ | $E_x$ | $E_y$ | $\mu_x$ | $\mu_y$ |
|---|---|---|---|---|---|---|---|---|---|
| $PC_3$ | e | 182.78 | 182.75 | 1.163 | 1.156 | 1.210 | 1.030 | 1.97 | 2.74 |
| $PC_3$ | h | 182.78 | 182.75 | 0.492 | 1.665 | 0.290 | 1.380 | 104.12 | 1.36 |
| $AsC_3$ | e | 142.95 | 142.19 | 2.238 | 2.012 | 1.011 | 0.970 | 0.63 | 0.76 |
| $AsC_3$ | h | 142.95 | 142.19 | 0.510 | 0.864 | 1.010 | 2.914 | 8.64 | 0.62 |
| $SbC_3$ | e | 106.63 | 106.61 | 0.393 | 0.473 | 3.010 | 2.310 | 1.48 | 2.09 |
| $SbC_3$ | h | 106.63 | 106.61 | 0.661 | 1.158 | 1.730 | 5.124 | 1.31 | 0.09 |
| $BiC_3$ | e | 86.28 | 86.30 | 0.341 | 0.341 | 6.370 | 6.430 | 0.39 | 0.38 |
| $BiC_3$ | h | 86.28 | 86.30 | 0.513 | 0.878 | 0.850 | 2.850 | 14.53 | 0.39 |

Taking $PC_3$ as an example, the hole mobility exhibits a strong directional dependence: it reaches $1.04 \times 10^5$ $cm^2$ $V^{-1}$ $s^{-1}$ along the $x$ direction, whereas along the $y$ direction it is only $1.4 \times 10^3$ $cm^2$ $V^{-1}$ $s^{-1}$, differing by nearly two orders of magnitude. This pronounced anisotropy primarily originates from the directional variation of the carrier effective mass and deformation potential, as summarized in Table 2. In contrast, the electron mobility of $PC_3$ is relatively isotropic, with comparable values of $1.97 \times 10^3$ and $2.74 \times 10^3$ $cm^2$ $V^{-1}$ $s^{-1}$ along the $x$ and $y$ directions, respectively. Furthermore, comparison of electron and hole mobilities shows that along the $x$ direction, holes ($1.04 \times 10^5$ $cm^2$ $V^{-1}$ $s^{-1}$) have significantly higher mobility than electrons ($1.97 \times 10^3$ $cm^2$ $V^{-1}$ $s^{-1}$), whereas the opposite trend occurs along the $y$ direction, where electrons ($2.74 \times 10^3$ $cm^2$ $V^{-1}$ $s^{-1}$) are more mobile than holes ($1.36 \times 10^3$ $cm^2$ $V^{-1}$ $s^{-1}$). The other three $XC_3$ compounds show similar transport behavior to $PC_3$. Such pronounced anisotropy and electron–hole asymmetry in carrier mobility are beneficial for the spatial separation of photogenerated carriers, suggesting that these materials hold strong potential for high-performance optoelectronic applications.

## 7. Photocatalytic water splitting properties

In photocatalytic water splitting, the built-in electric field in 2D polar materials can spatially separate photogenerated electrons and holes, thereby suppressing their recombination. Meanwhile, the field-induced band bending enables the hydrogen evolution reaction (HER) and oxygen evolution reaction (OER) to occur spontaneously at different active sites. Specifically, HER predominantly occurs at the CBM of the electron-rich surface, while OER occurs at the VBM of the hole-rich surface.[47–49]

To further clarify the relationship between the intrinsic polarization and carrier separation capability, we quantitatively evaluated $P_s$, the intrinsic electric field $E_{in}$, and the electrostatic potential difference between the two surfaces $\Delta\phi$. The calculated results are summarized in Table 2 and Fig. S5. It can be

Table 2 The bandgap $E_g$ (eV), first band-edge absorption peak $E_{abs}$ (eV), maximum carrier mobility $\mu_{max}$ ($10^3$ cm$^2$ V$^{-1}$ s$^{-1}$), spontaneous electric polarization $P_s$ (pC m$^{-1}$), intrinsic electric field $E_{in}$ (V Å$^{-1}$), electrostatic potential difference between the two surfaces $\Delta\phi$ (V) of $XC_3$

| $XC_3$ | $E_g$ | $E_{abs}$ | $\mu_{max}$ | $P_s$ | $E_{in}$ | $\Delta\phi$ |
|---|---|---|---|---|---|---|
| $PC_3$ | 2.13 | 3.45 | 104.12 | −3.1 | −0.52 | −0.35 |
| $AsC_3$ | 3.05 | 4.17 | 8.64 | 1.3 | 0.19 | 0.15 |
| $SbC_3$ | 3.11 | 3.59 | 2.09 | 3.9 | 0.49 | 0.44 |
| $BiC_3$ | 2.87 | 3.61 | 14.53 | 8.1 | 1.04 | 1.14 |

clearly seen that a larger polarization strength leads to a stronger built-in electric field and a larger surface potential difference. Such an enhanced internal electric field promotes the spatial separation of photogenerated carriers by driving electrons and holes toward opposite surfaces, thereby improving the carrier separation efficiency.

For $XC_3$ materials, the carbon atomic layer and the X atomic layer are defined as the upper and lower surfaces, respectively. Notably, $PC_3$ exhibits an opposite surface polarity compared with the other three compounds ($AsC_3$, $SbC_3$, and $BiC_3$). As shown in Fig. 4, the calculated VBM and CBM energy levels of all $XC_3$ compounds straddle the redox potentials of water over a wide pH range (0–10), indicating that they are thermodynamically capable of overall photocatalytic water splitting. Under neutral conditions (pH = 7), the electron reduction potential ($U_e$) follows the order $BiC_3$ (1.53 eV) > $SbC_3$ (1.06 eV) > $AsC_3$ (0.87 eV) > $PC_3$ (0.43 eV), suggesting that $BiC_3$ provides the strongest driving force for HER. In contrast, the hole oxidation potential ($U_h$) follows the order $SbC_3$ (1.21 eV) > $BiC_3$ (1.20 eV) > $AsC_3$ (1.07 eV) > $PC_3$ (0.81 eV), implying that $SbC_3$ is favorable for OER.

The $XC_3$ materials possess several advantages as photocatalysts for water splitting. Their high optical absorption coefficients, reaching up to $10^5$ cm$^{-1}$, enable efficient light harvesting in the ultraviolet-visible region, while their high carrier mobilities promote rapid transport of photogenerated carriers. Moreover, the intrinsic polarization generates a built-in electric field that effectively drives spatial charge separation and suppresses electron–hole recombination. These synergistic properties demonstrate the strong potential of $XC_3$ materials for efficient photocatalytic water splitting.

## 8. Discussion and conclusion

In summary, we have theoretically proposed a new family of polar semiconductors, $XC_3$ (X = P, As, Sb, Bi), formed by symmetric substitution of group-V elements into graphene. As summarized in Table 2, these monolayers exhibit excellent structural stability and outstanding optoelectronic performance, characterized by strong visible-to-near-UV absorption coefficients exceeding $10^5$ cm$^{-1}$ near the band edges. The enhanced optical absorption originates from pronounced band nesting and large transition dipole moments. Moreover, the spontaneous polar structure induces an intrinsic OOP electric field, while anisotropic carrier mobilities promote efficient separation and transport of photogenerated carriers. Combined with their favorable band-edge alignment for photocatalytic reactions, $XC_3$ monolayers hold great promise for solar-driven energy conversion. This work not only deepens the understanding of bandgap and polarity engineering in graphene-derived systems but also establishes $XC_3$ as a versatile

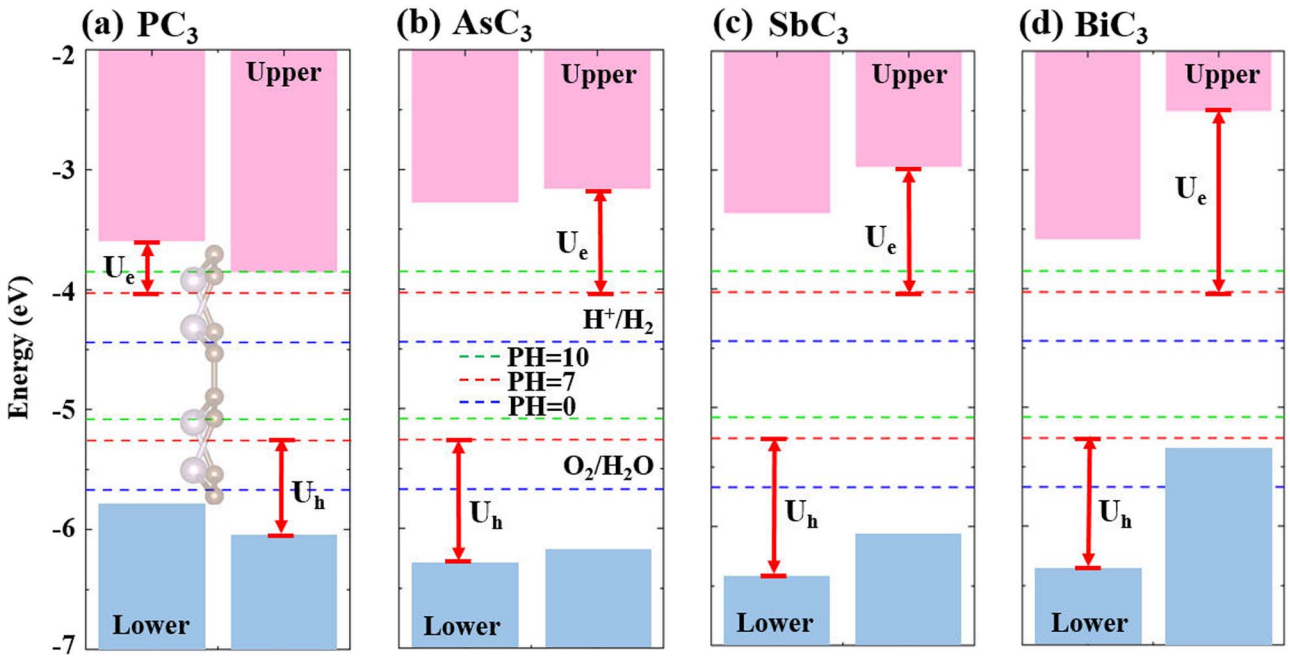


Fig. 4 Electronic band edge alignment of $XC_3$ with respect to the water redox potentials. The hydrogen and oxygen evolution potentials are shown as dashed lines.

platform for next-generation optoelectronic and photocatalytic applications.

## Conflicts of interest

There are no conflicts of interest to declare.

## Data availability

The data that support the findings of this study are available from the corresponding author upon reasonable request. All key results are reproducible based on the "Computational methods" in the main text.

Supplementary information (SI): structural stability analyses of $XC_3$, optical properties of $AsC_3$, electrostatic potential differences of $XC_3$, and the electronic band structures and optical absorption spectra of $SbC_3$ and $BiC_3$ with spin–orbit coupling (SOC) taken into account. See DOI: https://doi.org/10.1039/d6ra00272b.

## Acknowledgements

This work is supported by the National Natural Science Foundation of China (NSFC, Grant No. 12204330). Dr Botao Fu also thanks the Sichuan Normal University for financial support (Grant No. 341829001). The numerical computations were performed at the Hefei advanced computing center.

## References

1 A. Lherbier, A. R. Botello-Méndez and J.-C. Charlier, *Nano Lett.*, 2013, **13**, 1446.
2 E. V. Castro, K. Novoselov, S. Morozov, N. Peres, J. L. Dos Santos, J. Nilsson, F. Guinea, A. Geim and A. C. Neto, *Phys. Rev. Lett.*, 2007, **99**, 216802.
3 N. F. Martins, J. A. Laranjeira, K. A. Lima, L. A. Cabral, L. R. Junior and J. R. Sambrano, *Appl. Surf. Sci.*, 2025, 163737.
4 L. Li, Y. Yu, G. J. Ye, Q. Ge, X. Ou, H. Wu, D. Feng, X. H. Chen and Y. Zhang, *Nat. Nanotechnol.*, 2014, **9**, 372.
5 H. Liu, A. T. Neal, Z. Zhu, Z. Luo, X. Xu, D. Tománek and P. D. Ye, *ACS Nano*, 2014, **8**, 4033.
6 A. Castellanos-Gomez, L. Vicarelli, E. Prada, J. O. Island, K. Narasimha-Acharya, S. I. Blanter, D. J. Groenendijk, M. Buscema, G. A. Steele, J. Alvarez, *et al.*, *2D Mater.*, 2014, **1**, 025001.
7 J. D. Wood, S. A. Wells, D. Jariwala, K.-S. Chen, E. Cho, V. K. Sangwan, X. Liu, L. J. Lauhon, T. J. Marks and M. C. Hersam, *Nano Lett.*, 2014, **14**, 6964.
8 C. Kamal and M. Ezawa, *Phys. Rev. B: Condens. Matter Mater. Phys.*, 2015, **91**, 085423.
9 P. Ares, J. J. Palacios, G. Abellán, J. Gómez-Herrero and F. Zamora, *Adv. Mater.*, 2018, **30**, 1703771.
10 E. Aktürk, O. Ü. Aktürk and S. Ciraci, *Phys. Rev. B*, 2016, **94**, 014115.
11 S. Gao, Y. Sun, M. Pei, C. Yu, X. Wang and L. Zhai, *Chem. Phys.*, 2025, 112915.
12 P.-F. Liu, T. Bo, Z. Liu, O. Eriksson, F. Wang, J. Zhao and B.-T. Wang, *J. Mater. Chem. C*, 2018, **6**, 12689.
13 M. Naseri, *Appl. Surf. Sci.*, 2017, **423**, 566.
14 X. Fu, Y. Xie and Y. Chen, *Comput. Mater. Sci.*, 2018, **144**, 70.
15 X. Ma, J. Zhou, T. Yang, D. Li and Y. P. Feng, *Phys. Rev. Mater.*, 2021, **5**, 024005.
16 G. Wang, R. Pandey and S. P. Karna, *Nanoscale*, 2016, **8**, 8819.
17 B. Rajbanshi and P. Sarkar, *J. Phys. Chem. Lett.*, 2017, **8**, 747.
18 J. Guan, D. Liu, Z. Zhu and D. Tománek, *Nano Lett.*, 2016, **16**, 3247.
19 W. C. Tan, Y. Cai, R. J. Ng, L. Huang, X. Feng, G. Zhang, Y.-W. Zhang, C. A. Nijhuis, X. Liu and K.-W. Ang, *Adv. Mater.*, 2017, **29**, 1700503.
20 W. C. Tan, L. Huang, R. J. Ng, L. Wang, D. M. N. Hasan, T. J. Duffin, K. S. Kumar, C. A. Nijhuis, C. Lee and K.-W. Ang, *Adv. Mater.*, 2018, **30**, 1705039.
21 T. Yu, Z. Zhao, Y. Sun, A. Bergara, J. Lin, S. Zhang, H. Xu, L. Zhang, G. Yang and Y. Liu, *J. Am. Chem. Soc.*, 2019, **141**, 1599.
22 M. Kar, R. Sarkar, S. Pal and P. Sarkar, *Phys. Rev. B*, 2020, **101**, 195305.
23 X. Chen, J. Lin, Q. Lin, R. Li, G. Xia, W. Zou and X. Yu, *Phys. Rev. B*, 2022, **106**, 075402.
24 M. Zhong, W. Zeng, H. Qin, S.-H. Zhu, X.-H. Li, F.-S. Liu, B. Tang and Q.-J. Liu, *Phys. Chem. Chem. Phys.*, 2022, **24**, 10175.
25 W. Zhang, C. Chai, Q. Fan, Y. Song and Y. Yang, *ChemPhysChem*, 2021, **22**, 1124.
26 H. Zhang, Y. Tang, X. Zhou, Y. Sun, Q. Liang, K. Zhao and Z. Wu, *Ceram. Int.*, 2024, **50**, 34974.
27 M. Gmitra and J. Fabian, *Phys. Rev. B: Condens. Matter Mater. Phys.*, 2015, **92**, 155403.
28 A. Weston, E. G. Castanon, V. Enaldiev, F. Ferreira, S. Bhattacharjee, S. Xu, H. Corte-León, Z. Wu, N. Clark, A. Summerfield, *et al.*, *Nat. Nanotechnol.*, 2022, **17**, 390.
29 N. Zhou, X. Wu, H. Wen, J. Cao, H. Li and R. Liu, *Ceram. Int.*, 2025, **50**, 34974–34986.
30 N. T. Hung, T. Nguyen, V. Van Thanh, S. Wang, R. Saito and M. Li, *J. Phys. D: Appl. Phys.*, 2024, **57**, 333002.
31 G. Kresse and J. Hafner, *Phys. Rev. B: Condens. Matter Mater. Phys.*, 1993, **47**, 558.
32 G. Kresse and J. Hafner, *Phys. Rev. B: Condens. Matter Mater. Phys.*, 1994, **49**, 14251.
33 G. Kresse and J. Furthmüller, *Comput. Mater. Sci.*, 1996, **6**, 15.
34 G. Kresse and J. Furthmüller, *Phys. Rev. B: Condens. Matter Mater. Phys.*, 1996, **54**, 11169.
35 J. P. Perdew, K. Burke and M. Ernzerhof, *Phys. Rev. Lett.*, 1996, **77**, 3865.
36 A. V. Krukau, O. A. Vydrov, A. F. Izmaylov and G. E. Scuseria, *J. Chem. Phys.*, 2006, **125**, 224106.
37 H. J. Monkhorst and J. D. Pack, *Phys. Rev. B*, 1976, **13**, 5188.
38 J. Mahmood, E. K. Lee, M. Jung, D. Shin, H.-J. Choi, J.-M. Seo, S.-M. Jung, D. Kim, F. Li, M. S. Lah, *et al.*, *Proc. Natl. Acad. Sci. U. S. A.*, 2016, **113**, 7414.
39 H. Yao, Q. Wang, J. Li, W. Cai, Y. Wei, B. Wang and J. Wang, *Phys. Chem. Chem. Phys.*, 2020, **22**, 9477.

40 See SI for stability assessments (binding energy, formation energy, phonon spectra, AIMD, ELF, elastic constants), electronic/optical properties (absorption coefficient, JDOS, TDM, local gap distribution) of $XC_3$ (X = P, As, Sb, Bi) monolayers, SOC effect for $SbC_3$ and BiC.
41 M. Gajdoš, K. Hummer, G. Kresse, J. Furthmüller and F. Bechstedt, *Phys. Rev. B: Condens. Matter Mater. Phys.*, 2006, **73**, 045112.
42 M. Fox, *Optical Properties of Solids*, Oxford University Press, 2010, vol. 3.
43 L.-R. Zou, D.-D. Sang, Y. Yao, X.-T. Wang, Y.-Y. Zheng, N.-Z. Wang, C. Wang and Q.-L. Wang, *Rare Met.*, 2023, **42**, 17.
44 R. Alicki, *Int. J. Theor. Phys.*, 1977, **16**, 351.
45 Z. Li, X. Ma, H. Pan, H. Chu, Z. Pan, Y. Li, S. Zhao and D. Li, *Opt. Express*, 2023, **31**, 19666.
46 J. Qiao, X. Kong, Z.-X. Hu, F. Yang and W. Ji, *Nat. Commun.*, 2014, **5**, 4475.
47 T. Su, Q. Shao, Z. Qin, Z. Guo and Z. Wu, *ACS Catal.*, 2018, **8**, 2253.
48 X. Li, Z. Li and J. Yang, *Phys. Rev. Lett.*, 2014, **112**, 018301.
49 H. Wu, W. Li, Q. Li and B. Fu, *Nanoscale*, 2025, **17**, 21157–21165.